

Molecular streaming and its voltage control in ångström-scale channels

T. Mouterde^{1,5}, A. Keerthi^{2,3,5}, A. R. Poggioli¹, S. A. Dar^{2,3,4}, A. Siria¹, A. K. Geim^{2,3*}, L. Bocquet^{1*} & B. Radha^{2,3*}

Over the past decade, the ability to reduce the dimensions of fluidic devices to the nanometre scale (by using nanotubes^{1–5} or nanopores^{6–11}, for example) has led to the discovery of unexpected water- and ion-transport phenomena^{12–14}. More recently, van der Waals assembly of two-dimensional materials¹⁵ has allowed the creation of artificial channels with ångström-scale precision¹⁶. Such channels push fluid confinement to the molecular scale, wherein the limits of continuum transport equations¹⁷ are challenged. Water films on this scale can rearrange into one or two layers with strongly suppressed dielectric permittivity^{18,19} or form a room-temperature ice phase²⁰. Ionic motion in such confined channels²¹ is affected by direct interactions between the channel walls and the hydration shells of the ions, and water transport becomes strongly dependent on the channel wall material²². We explore how water and ionic transport are coupled in such confinement. Here we report measurements of ionic fluid transport through molecular-sized slit-like channels. The transport, driven by pressure and by an applied electric field, reveals a transistor-like electrohydrodynamic effect. An applied bias of a fraction of a volt increases the measured pressure-driven ionic transport (characterized by streaming mobilities) by up to 20 times. This gating effect is observed in both graphite and hexagonal boron nitride channels but exhibits marked material-dependent differences. We use a modified continuum framework accounting for the material-dependent frictional interaction of water molecules, ions and the confining surfaces to explain the differences observed between channels made of graphene and hexagonal boron nitride. This highly nonlinear gating of fluid transport under molecular-scale confinement may offer new routes to control molecular and ion transport, and to explore electromechanical couplings that may have a role in recently discovered mechanosensitive ionic channels²³.

Our devices (Fig. 1) were ångström-scale channels on a Si/SiN substrate, fabricated as previously described^{16,21} through van der Waals assembly of two (approximately 10 nm and 150 nm) thin crystals of graphite separated by strips of bilayer graphene. Each device had $N = 200$ channels of height $h_0 \approx 6.8$ Å, width $w = 130$ nm and length L of a few micrometres (see Methods section ‘Device fabrication’ and Extended Data Fig. 1). The channels were assembled on top of a micro-metre opening etched in the Si/SiN wafer that served as entry to the fluidic channels, with the exit on the other side of the wafer (Fig. 1). The channels connected two macroscopic reservoirs filled with KCl solutions of concentration c and containing chlorinated Ag/AgCl electrodes for electrical current measurements. As previously reported²¹, the net current I at high salt concentration is typically of the order of a few picoamps per channel for applied voltages of a few tens of millivolts and varies linearly with voltage and concentration as expected for this ultra-confined system with small surface charge²¹. In this study, we focus on the ionic current driven by the pressure drop ΔP and the effect of the additional potential difference ΔV applied along the channel. For this, ΔV was controlled by a patch-clamp amplifier (ground electrode

is on the top side) with a current resolution of 0.1 pA; and pressure by a pump connected to the reservoir (Methods section ‘Streaming current measurements’). We applied the pressure in both directions across the channel and found no influence on the reported results (see Extended Data Fig. 2; pressure applied from the bottom side in Fig. 1 is denoted as positive). Control experiments used similar devices but without channels and yielded no current upon application of ΔP or ΔV , confirming that our devices were structurally stable and, for example, did not delaminate under pressure (see Methods section ‘Streaming current measurements’ and Extended Data Fig. 3).

This setup (Fig. 1) allows us to measure the pressure driven component of the ionic current, referred to as the streaming current $I_{\text{str}} = I(\Delta P, \Delta V) - I(0, \Delta V)$, which provides an indirect measure of water flow under confinement. Figure 2 illustrates the behaviour in the absence of applied bias ($\Delta V = 0$), with Fig. 2a showing the time response of I_{str} when stepping ΔP up to 125 mbar in 25 mbar increments. Each step lasts 20 s, and the delay between successive steps is 20 s. After an initial overshoot, I_{str} rapidly reaches a steady state and, once the pressure is released, quickly returns to zero. The measured current is positive for positive applied pressures, which corresponds to a flow conveying a net positive charge that gradually increases with the pressure gradient, $\Delta P/L$. This is consistent with the reduction in chloride mobility as compared to that of potassium under strong confinement²¹ (right panel of Fig. 1).

We find that, for concentrations between 1 mM and 300 mM, the steady-state current reached after each pressure increment (Fig. 2a) increases linearly with the driving force, that is, the pressure gradient (Fig. 2b). From the measured slopes, we calculate the streaming (electroosmotic) mobility $\mu = I_{\text{str}}/(NA\Delta P/L)$, where $A = wh_0$ is the slit cross-sectional area. The streaming mobility weakly depends on salt concentration (Fig. 2c), varying by less than 50% if c is increased by a factor of 300. However, the absolute value of μ is surprisingly high: it is of the order of $10^{-7} \text{ m}^2 \text{ V}^{-1} \text{ s}^{-1}$, which is in the range of the bulk potassium electrophoretic mobility $\mu_{\text{K}+} = 7.6 \times 10^{-8} \text{ m}^2 \text{ V}^{-1} \text{ s}^{-1}$ and an order of magnitude larger than streaming mobilities reported in the literature (for example, the streaming mobility for SiO₂ channels is about $0.1\mu_{\text{K}+}$). As a comparison, we consider the measured streaming mobility in terms of the corresponding zeta potential, which has the dimension of an electrostatic potential. Using bulk water properties (viscosity $\eta = 1 \text{ mPa s}$ and dielectric permittivity $\epsilon \approx 80$) gives us an apparent zeta potential, $\zeta = -\mu\eta/\epsilon\varepsilon_0$, of roughly -0.4 V, at least ten times the typical values in the literature^{2,24,25} which are of the order of $kT/e \approx 25 \text{ mV}$. Recent studies of confined water indicate that its out-of-plane relative permittivity can be markedly suppressed¹⁹ to $\epsilon_{\text{reduced}} \approx 2$ whereas η remains close to the bulk value¹⁶, which would translate into an even larger apparent ζ of -16 V. However, in our opinion, such a large apparent zeta potential does not reflect an anomalously high surface potential of the graphite but instead the high streaming mobility arising from the unusually fast transport of water, and hence hydrated ions, at molecular distances from the channel surfaces.

¹Laboratoire de Physique de l'Ecole normale supérieure, ENS, Université PSL, CNRS, Sorbonne Université, Université Paris-Diderot, Sorbonne Paris Cité, Paris, France. ²School of Physics and Astronomy, University of Manchester, Manchester, UK. ³National Graphene Institute, University of Manchester, Manchester, UK. ⁴Department of Basic Sciences and Humanities, University of Engineering and Technology (KSK), Lahore, Pakistan. ⁵These authors contributed equally: T. Mouterde, A. Keerthi.

*e-mail: geim@manchester.ac.uk; lyderic.bocquet@ens.fr; radha.oya@manchester.ac.uk

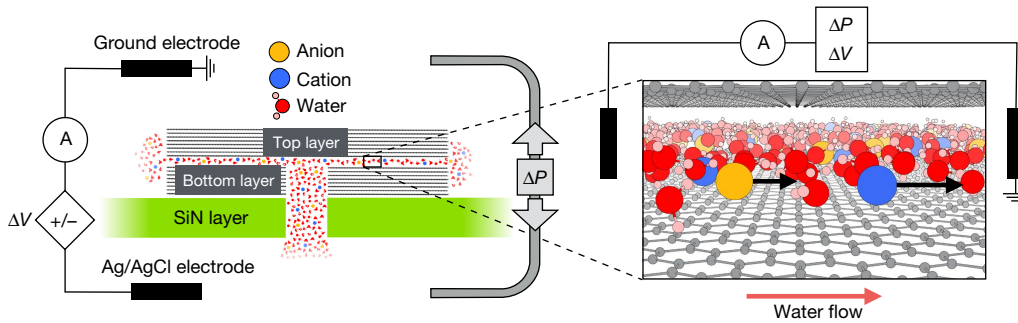


Fig. 1 | Experimental setup for pressure- and voltage-driven current. Schematic: ångström channels (fabricated on a Si/SiN wafer) separate two reservoirs containing KCl solutions. The entry and exit of the channel are on either side of the wafer. We set the voltage ΔV and the pressure ΔP along the channels and monitored the resulting current I . Right panel,

Figure 3 shows pressure-driven streaming currents measured under different applied voltage biases, allowing us to explore how the pressure-induced current couples to electric forces at these molecular scales. Figure 3a shows the time response of I_{str} when applying pressure and ΔV simultaneously, revealing a considerable coupling between them in that I_{str} increases by more than 100% for $\Delta V = 50$ mV as compared with its value at zero ΔV . As illustrated in Fig. 3b, the effects of ΔP and ΔV do not simply add: although the current always remains proportional to the pressure gradient, independent of applied bias, the slope of this linear dependence—the streaming mobility $\mu(\Delta V)$ —varies with ΔV according to $I_{\text{str}} = \mu(\Delta V) \times A \times N \times \Delta P/L$. The linear dependence of streaming current on pressure highlights that it originates from the hydrodynamic transport of ions, while its voltage dependence indicates an unexpected interplay between mechanical and electric driving forces. To disentangle these effects further, we plot in Fig. 3d mobilities measured in graphite channels and normalized by μ_{K+} as a function of ΔV and c .

We also compare the streaming effects in graphite channels with those of similar channels made from hexagonal boron nitride (hBN). In terms of crystal structure and atomic flatness, hBN is an analogue of graphite²⁶ but electrically insulating. Our hBN devices were fabricated using the same procedures as before and had the same parameters including h_0 , and their behaviour was similar to that of graphite devices in that I_{str} varied linearly with ΔP (see Fig. 3c, Extended Data Figs. 2 and 4) and with a slope (streaming mobility μ) that was tunable by applied bias. But the dependence of $\mu(\Delta V)$ differs greatly between the two materials: μ shows a quadratic response to electric bias for graphite (Fig. 3d), whereas it is essentially linear over the entire

illustration of ions moving in water under strong confinement (only one layer of top and bottom graphite walls is shown for clarity). Positive streaming currents indicate that potassium ions move faster than chloride ions inside the channel.

measurement range for hBN (Fig. 3e). The data can be described for graphite by

$$\mu(\Delta V) = \mu_0 \left[1 + \alpha \left(\frac{\Delta V - V_{\min}}{V_{\text{ref}}} \right)^2 \right] \quad (1)$$

and for hBN by

$$\mu(\Delta V) = \mu_0 \left[1 + \beta \frac{\Delta V}{V_{\text{ref}}} \right] \quad (2)$$

where $V_{\text{ref}} = kT/e \approx 25$ mV is the thermal voltage, μ_0 is a mobility, and α and β are dimensionless parameters accounting for the voltage response. Typically, V_{\min} is found to be of the order of V_{ref} and decreases with c ; the voltage susceptibility α increases linearly with concentration (Extended Data Figs. 5a,b), reaching a value close to unity for high $c = 300$ mM. The characteristic mobility μ_0 is typically of the order of μ_{K+} for both systems. However, similar to α in graphite, the bias susceptibility β for hBN increases linearly with c (Extended Data Fig. 5c). Owing to the linear voltage coupling, the sign of the streaming current for hBN can be inverted for negative biases (Extended Data Fig. 4). For both materials, the sensitivity of I_{str} to voltage bias is very large, in contrast to other known control or gating mechanisms^{27–31}. For graphite channels, a relatively small voltage ($\Delta V \approx 75$ mV) yields streaming mobilities which are up to about 20 times as large as the bulk potassium mobility, taken as a reference. This corresponds to zeta potentials up to 2 V assuming the bulk water properties, and about 100 V if using the

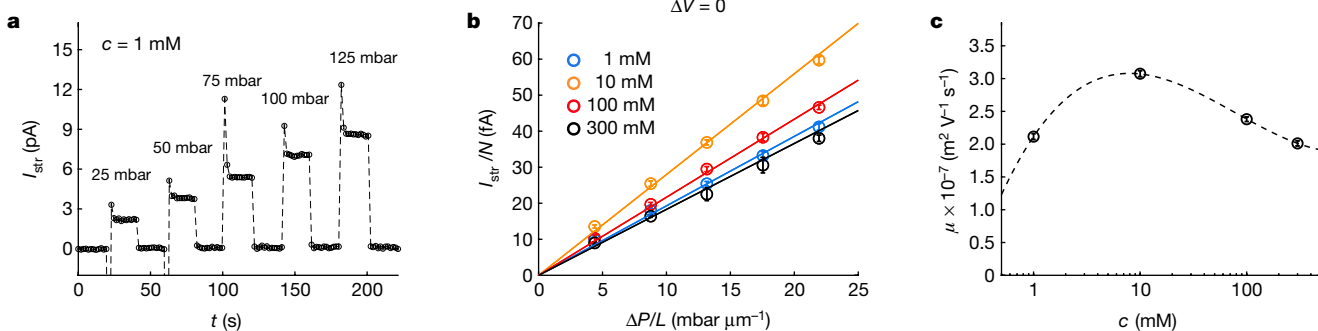


Fig. 2 | Pressure-driven current without applying bias. **a**, I_{str} as a function of time for graphite channels; $c = 1$ mM; $L = 5.7 \pm 0.1$ μm . Current overshoots once the pressure is applied, and we consider only the steady-state regime in this study. **b**, Streaming current per channel, I_{str}/N , as a function of the pressure gradient $\Delta P/L$ for channels in **a**, and with different KCl concentrations c . For each c , the line corresponds to

the best linear fit. **c**, Electro-osmotic mobility μ as a function of the KCl concentration (linear-logarithmic coordinates; dashed line is a guide to the eye). Error bars represent: **a**, error in the currents measured during temporal evolution (± 0.1 pA); **b**, standard error; **c**, uncertainty in the fit value. Three devices were measured and showed the same behaviour.

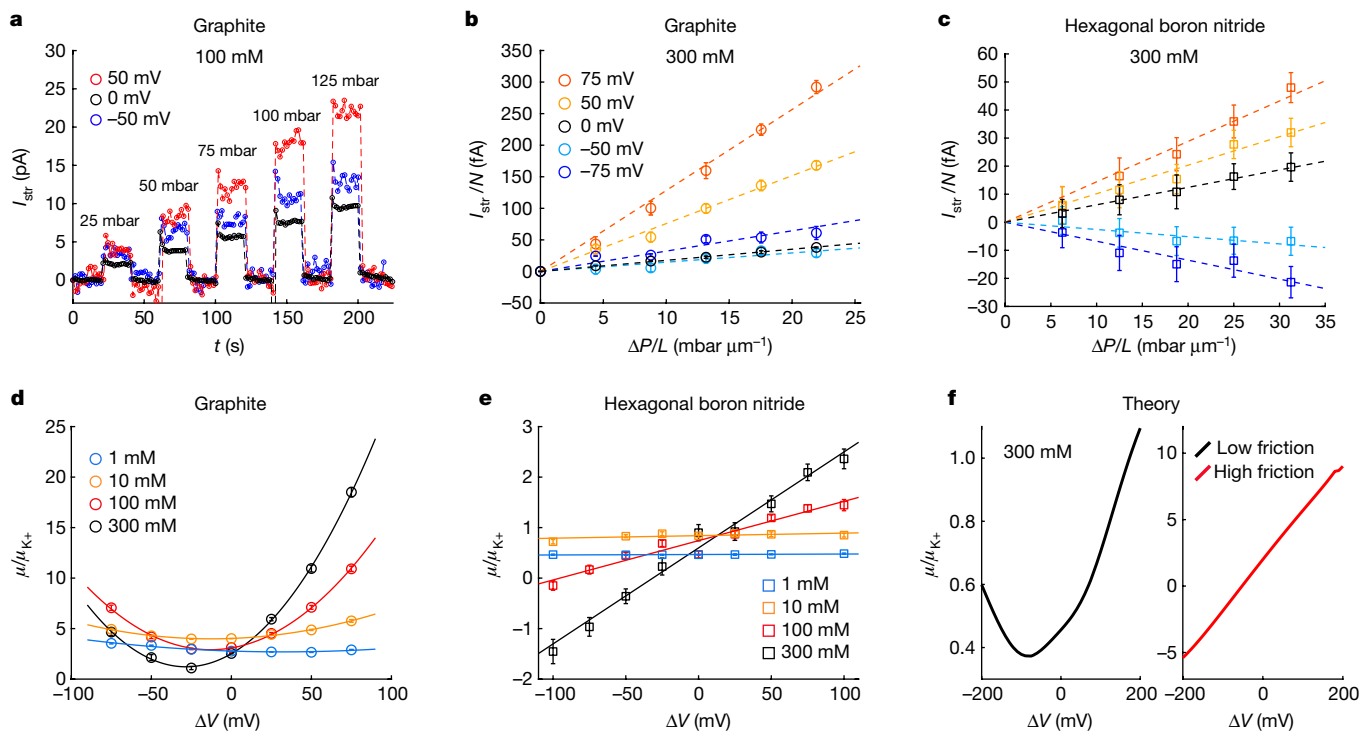


Fig. 3 | Streaming current for different biases and channel materials.

a, Pressure-driven I_{str} for a graphite device at different ΔV . $L = 5.7 \pm 0.1 \mu\text{m}$; KCl concentration, 100 mM. The pressure applied for 20 s intervals is gradually increased to 125 mbar in 25 mbar steps. **b**, Streaming current per channel for the same device as a function of $\Delta P/L$ (bias ΔV ranges from -75 to 75 mV; colour coded). **c**, Streaming current for similar devices but with hBN walls; same experiments and colour coding as in **a** and **b**. **d**, Streaming mobility (normalized by the K^+ electrophoretic mobility) as a function of ΔV for different KCl concentration for the graphite devices. Curves are the quadratic fits. **e**, Same as **d** but with hBN

channels. Linear fits; $L = 16 \pm 0.1 \mu\text{m}$. **f**, Extended PNP prediction for the streaming mobility using different friction coefficients between the water, ions and wall, with a factor of 100 between low and high friction. Low friction reproduces the quadratic gating observed for graphite (**d**), while high friction leads to the linear gating observed for hBN (**e**). Detailed parameters and geometry used in the model are given in the Methods section ‘Extended Poisson–Nernst–Planck theory’ and Extended Data Figs. 6–10. Error bars represent: **a–c**, measurement uncertainty; **d, e**, uncertainty in the fit value.

confined-water relative permittivity $\varepsilon_{\text{reduced}}$. Although the effect is still large for hBN, it is substantially smaller than that in graphite channels. This observation echoes the smaller slip length for water on hBN as compared with graphite^{4,22,32}.

Taken together, our findings indicate that the applied bias voltage acts as a gate for pressure-driven streaming currents. Although it is tempting to rationalize this behaviour in terms of capacitive gating, as assumed, for example, for flowFET-type devices (fluidic analogues of field-effect transistors)²⁷, such an explanation fails to capture key experimental observations such as the contrasting voltage dependence of the gating for graphite and hBN. Any capacitive gating explanation also neglects the electrohydrodynamic coupling between ion and water transport under ångström-scale confinement, which is usually described in terms of the Poisson–Nernst–Planck–Stokes (PNPS) framework commonly used to describe ionic transport in biological or artificial channels. But this PNPS model is also unable to account for all our observations, in particular the qualitatively different bias dependence of μ seen for graphite versus hBN as summarized in equations (1) and (2). We attribute this to the strong confinement encountered in our devices, which renders the Stokes equation irrelevant when describing flow within the water/ion layer, owing to strong and direct interactions of the moving ions and water molecules with the confining walls.

We account for this effect by considering friction between water, ions and the walls, which we capture by an effective water–wall friction that depends on ion concentrations. This may be described as $\lambda_w(\rho_+, \rho_-) = \lambda_0 + h_0(\kappa_+ \rho_+ + \kappa_- \rho_-)$, where λ_0 is the bare (ion-free) friction coefficient for water, κ_\pm are coefficients characterizing the ions’ contribution to the friction, and ρ_\pm are the ion concentrations. (The full model for our channel geometry is detailed in the Methods section ‘Extended Poisson–Nernst–Planck theory’, and in Extended Data

Figs. 6 to 10.) The resultant extended Poisson–Nernst–Planck (PNP) model qualitatively reproduces most of the experimental observations, leading to streaming currents that are linear in ΔP (Extended Data Fig. 7) and reproducing the large increase in streaming mobility under applied bias (Fig. 3f) that is in contrast to the standard consequences of concentration polarization. As illustrated in Fig. 3f, the model also yields different functional dependences $\mu(\Delta V)$ according to the friction behaviour of both water and ions on the different materials: low friction between water molecules and ions and the channel wall leads to a quadratic gating of the streaming mobility as observed for graphite, whereas large friction results in an essentially linear dependence as observed for hBN. The model and underlying theory indicate that this behaviour results from a subtle and intertwined effect of concentration dependent flow and ion concentration profile across the channels in the presence of voltage. Accordingly, the different material response observed in Fig. 3 for channels made from hBN and graphite can be traced back to the difference of molecular friction of water and ions on these two materials. This is in agreement with expectations for the friction of water on these two materials^{4,22,32}. A remarkable feature of this framework is that the observed nonlinear bias response thus has its roots in the fundamental nature of interactions between confining walls, water molecules and ions. For instance, the minimum mobility seen in Fig. 3d arises from the slight asymmetry in device geometry which is at the origin of different frictions (induced by the confinement) and modifies locally the transport rates of ions on each side. Although the simple model reproduced our experimental results qualitatively (Extended Data Figs. 8 to 10), it cannot account for the large amplitude of the bias voltage effect seen with graphite channels. Better agreement will require more comprehensive evaluation of the effects of strong confinement (including the suppressed dielectric constant),

which are expected to modify not only water and ion dynamics but also the adsorption of the ions³³. Furthermore, the metallicity of graphite can substantially modify ionic interactions and thereby ion concentrations. We anticipate that extending ab initio molecular simulations of water friction²², to include the effect of ions, will provide further insight beyond the simple picture proposed here.

Our experimental system allows us to probe purely two-dimensional flow of water and ions, a configuration very different from the one-dimensional transport through nanotubes. Thanks to the lateral extension of the ångström channels, streaming currents under molecular confinement become measurable. Hence, such devices are an interesting platform in which to mimic the behaviour of biological channels in terms of stimuli responsive behaviour such as voltage gating, where ions are driven through ångström-scale confinement by coupled osmotic pressure and electric forcing. This is of relevance for gaining new insights into the electromechanical coupling at the root of the mechanosensitivity observed in recently discovered biological ionic channels²³ (TRAAT, TREK, PIEZO). Furthermore, the observed friction-based electric gating opens a new route to achieve flow-control under extreme confinement where small voltages induce strong responses, which would constitute an important step towards building nanofluidic circuits responding to external stimuli.

Online content

Any methods, additional references, Nature Research reporting summaries, source data, statements of data availability and associated accession codes are available at <https://doi.org/10.1038/s41586-019-0961-5>.

Received: 20 July 2018; Accepted: 17 December 2018;
Published online 6 March 2019.

1. Fornasiero, F. et al. Ion exclusion by sub-2-nm carbon nanotube pores. *Proc. Natl Acad. Sci. USA* **105**, 17250–17255 (2008).
2. Siria, A. et al. Giant osmotic energy conversion measured in a single transmembrane boron nitride nanotube. *Nature* **494**, 455–458 (2013).
3. Secchi, E., Nigués, A., Jubin, L., Siria, A. & Bocquet, L. Scaling behavior for ionic transport and its fluctuations in individual carbon nanotubes. *Phys. Rev. Lett.* **116**, 154501 (2016).
4. Secchi, E. et al. Massive radius-dependent flow slippage in carbon nanotubes. *Nature* **537**, 210–213 (2016).
5. Tunuguntla, R. H. et al. Enhanced water permeability and tunable ion selectivity in subnanometer carbon nanotube porins. *Science* **357**, 792–796 (2017).
6. Garaj, S. et al. Graphene as a subnanometre trans-electrode membrane. *Nature* **467**, 190–193 (2010).
7. Joshi, R. K. et al. Precise and ultrafast molecular oxide membranes. *Science* **343**, 752–754 (2014).
8. Jain, T. et al. Heterogeneous sub-continuum ionic transport in statistically isolated graphene nanopores. *Nat. Nanotechnol.* **10**, 1053–1057 (2015).
9. Feng, J. et al. Single-layer MoS₂ nanopores as nanopower generators. *Nature* **536**, 197–200 (2016).
10. Hong, S. et al. Scalable graphene-based membranes for ionic sieving with ultrahigh charge selectivity. *Nano Lett.* **17**, 728–732 (2017).
11. Abraham, J. et al. Tunable sieving of ions using graphene oxide membranes. *Nat. Nanotechnol.* **12**, 546–550 (2017).
12. Eijkel, J. C. T. & van den Berg, A. Nanofluidics: what is it and what can we expect from it? *Microfluid. Nanofluidics* **1**, 249–267 (2005).
13. Schoch, R. B., Han, J. & Renaud, P. Transport phenomena in nanofluidics. *Rev. Mod. Phys.* **80**, 839–883 (2008).
14. Howorka, S. & Siwy, Z. Nanopore analytics: sensing of single molecules. *Chem. Soc. Rev.* **38**, 2360–2384 (2009).
15. Geim, A. K. & Grigorieva, I. V. Van der Waals heterostructures. *Nature* **499**, 419–425 (2013).
16. Radha, B. et al. Molecular transport through capillaries made with atomic-scale precision. *Nature* **538**, 222–225 (2016).

17. Bocquet, L. & Charlaix, E. Nanofluidics, from bulk to interfaces. *Chem. Soc. Rev.* **39**, 1073–1095 (2010).
18. Schlaich, A., Knapp, E. W. & Netz, R. R. Water dielectric effects in planar confinement. *Phys. Rev. Lett.* **117**, 048001 (2016).
19. Fumagalli, L. et al. Anomalously low dielectric constant of confined water. *Science* **360**, 1339–1342 (2018).
20. Albara-Siller, G. et al. Square ice in graphene nanocapillaries. *Nature* **519**, 443–445 (2015).
21. Esfandiar, A. et al. Size effect in ion transport through angstrom-scale slits. *Science* **358**, 511–513 (2017).
22. Tocci, G., Joly, L. & Michaelides, A. Friction of water on graphene and hexagonal boron nitride from ab initio methods: very different slippage despite very similar interface structures. *Nano Lett.* **14**, 6872–6877 (2014).
23. Coste, B. et al. Piezo proteins are pore-forming subunits of mechanically activated channels. *Nature* **483**, 176–181 (2012).
24. Sze, A., Erickson, D., Ren, L. & Li, D. Zeta-potential measurement using the Smoluchowski equation and the slope of the current-time relationship in electroosmotic flow. *J. Colloid Interface Sci.* **261**, 402–410 (2003).
25. Geismann, C., Yaroshchuk, A. & Ulbricht, M. Permeability and electrokinetic characterization of poly(ethylene terephthalate) capillary pore membranes with grafted temperature-responsive polymers. *Langmuir* **23**, 76–83 (2007).
26. Keerthi, A. et al. Ballistic molecular transport through two-dimensional channels. *Nature* **558**, 420–424 (2018).
27. Schasfoort, R. B. M., Schlautmann, S., Hendrikse, J. & van den Berg, A. Field-effect flow control for microfabricated fluidic networks. *Science* **286**, 942–945 (1999).
28. Kim, S. J., Li, L. D. & Han, J. Amplified electrokinetic response by concentration polarization near nanofluidic channel. *Langmuir* **25**, 7759–7765 (2009).
29. Jiang, Z. & Stein, D. Charge regulation in nanopore ionic field-effect transistors. *Phys. Rev. E* **83**, 031203 (2011).
30. Karnik, R. et al. Electrostatic control of ions and molecules in nanofluidic transistors. *Nano Lett.* **5**, 943–948 (2005).
31. Pang, P., He, J., Park, J. H., Krstić, P. S. & Lindsay, S. Origin of giant ionic currents in carbon nanotube channels. *ACS Nano* **5**, 7277–7283 (2011).
32. Xie, Q. et al. Fast water transport in graphene nanofluidic channels. *Nat. Nanotechnol.* **13**, 238–245 (2018).
33. Futamura, R. et al. Partial breaking of the Coulombic ordering of ionic liquids confined in carbon nanopores. *Nat. Mater.* **16**, 1225–1232 (2017).

Acknowledgements T.M. and L.B. acknowledge funding from ANR project Neptune. B.R. acknowledges a Royal Society Fellowship, a L’Oreal Fellowship for Women in Science, and EPSRC grant EP/R013063/1. A.S. acknowledges funding from the European Union’s Horizon 2020 (EU H2020) Framework Programme/ERC Starting Grant agreement number 637748—NanoSOFT. L.B. acknowledges funding from the EU H2020 Framework Programme/ERC Advanced Grant agreement number 785911—Shadoks. A.R.P. acknowledges funding from the EU H2020 Framework Programme/European Training Programme 674979—NanoTRANS. S.A.D. was funded by a scholarship from the University of Engineering and Technology, Lahore Pakistan. A.K., B.R. and A.K.G. were supported by Lloyd’s Register Foundation and European Research Council (ARTIMATTER). T.M. thanks S. Blin and H. Yoshida for assistance.

Reviewer information *Nature* thanks Rohit Karnik and the other anonymous reviewer(s) for their contribution to the peer review of this work.

Author contributions B.R., L.B. and A.S. designed and directed the project. A.K., B.R. and S.A.D. fabricated the devices. T.M. performed the measurements and their analysis. A.R.P., T.M. and L.B. provided theoretical support. T.M., L.B., B.R., A.K. and A.R.P. wrote the manuscript with inputs from A.K.G. All authors contributed to discussions.

Competing interests The authors declare no competing interests.

Additional information

Extended data is available for this paper at <https://doi.org/10.1038/s41586-019-0961-5>.

Reprints and permissions information is available at <http://www.nature.com/reprints>.

Correspondence and requests for materials should be addressed to A.K.G., L.B. or B.R.

Publisher’s note: Springer Nature remains neutral with regard to jurisdictional claims in published maps and institutional affiliations.

© The Author(s), under exclusive licence to Springer Nature Limited 2019

METHODS

Device fabrication. Our devices were fabricated following previously reported procedures^{16,21}. In brief, a free-standing silicon nitride (SiN) membrane of around 500 nm in thickness provided mechanical support and served to separate the two reservoirs connected by the channels. On the membrane, a rectangular hole of approximately 3 μm × 26 μm was defined by lithography and plasma etching. The channels were made by van der Waals assembly of three layers—bottom, spacer, top—of 2D crystals such as graphite or hBN. First, a bottom layer of around 10- to 50-nm-thick graphite or hBN was transferred onto the hole in the SiN membrane and etched from the back side, which projected the hole into the bottom layer. Following this, pre-patterned bilayer graphene spacers (about 6.8 Å thick) in the form of parallel ribbons about 130 nm wide and separated also by about 130 nm were transferred onto the bottom crystal and aligned perpendicular to the long axis of the rectangular hole. Finally, a thick (about 100 nm to 150 nm) top crystal of graphite or hBN was transferred onto the spacers covering the hole (Extended Data Fig. 1). The top crystal defined the length of the channels that formed on both sides of the hole.

Streaming current measurements. Extended Data Fig. 3a–c shows the streaming current measurements as a function of the applied pressure for a sample containing no channels (varying from 0 to 250 mbar). The pressure is applied via a pressure pump (AF1, Elveflow) (we denote a positive ΔP for a pressure applied through the hole on SiN) and ΔV is controlled via a patch-clamp amplifier (Axopatch 200B, Molecular Devices) with the ground electrode on the top side. For a sample containing no channels, we did not detect any significant current. Extended Data Fig. 3d–f compares the streaming current measured for the control sample and a graphite device containing 200 channels. In the case of graphite channels, the streaming current is four orders of magnitude larger than the noise measured in the control sample.

To investigate the pressure dependence of the streaming current, we performed the streaming current measurements applying the pressure successively on each side of the membrane. The inversion of the pressure gradient fully reverts the streaming current sign as presented in Extended Data Fig. 2; this confirms the linear dependence of the streaming current on the mechanical forcing.

The molecular streaming current I_{str} as a function of the pressure gradient $\Delta P/L$ is shown in Extended Data Fig. 4 for both graphite and hBN devices and for different KCl concentrations and applied voltages. The streaming current varies linearly with the driving force $\Delta P/L$.

Extended Poisson–Nernst–Planck theory. Governing equations. At scales greater than about 1 nm, the influence of water motion on the ionic fluxes is accounted for by (1) appending Stokes' equation for the solvent velocity to the typical PNP description of the ionic transport and (2) including an ionic drift velocity set by the balance of forces between the electric force on the individual ion and the frictional force between the ion and water in the Nernst–Planck parameterization of the solute fluxes. Both assumptions are inapplicable here owing to the extreme confinement scale of the channels considered, which approaches the diameter of the water molecules and hydrated ions themselves. In particular, application of the Stokes equation to predict the hydrodynamic velocity relies on the assumption of a spatially homogeneous and isotropic scalar viscosity, an assumption that cannot be valid when a single layer of water molecules is present. A priori, we would expect strong interaction between the ions and walls, and the water molecules and walls. The former supposition is supported by the results of ref. ²¹, where the chloride mobility in both graphite and hBN devices of the type examined here was observed to be reduced by approximately 65% compared with bulk. The latter is supported by the present results when combined with the simple, first-principles model detailed below.

As noted above, the traditional ionic and hydrodynamic force balances, leading to the typical parameterization of the drift velocity and the Stokes equation, respectively, can no longer be sufficient to describe the coupled ion–water transport in one-to-two layers confinement owing to the substantial interaction with the confining material. As a simple first-principles approach, we consider the force balances on the individual ions and on a control volume of infinitesimal length along the slit containing both ions and water molecules. We include three phenomenological forces, the frictional interactions of (1) water with walls, (2) ions with walls and (3) ions with water. We emphasize that this is the simplest possible coherent approach to capture the modification in the qualitative behaviour of the ion dynamics owing to the extreme confinement. Quantifying the friction to achieve a more quantitatively accurate treatment would probably necessitate more in-depth modelling (such as ab initio molecular dynamics).

Including the ion–wall interaction, a force balance on an individual ion gives:

$$0 = \pm e(-\partial_x \phi) - \xi_{\pm}(v_{\pm} - v_w) - \lambda_{\pm} v_{\pm} \quad (3)$$

where v_{\pm} is the velocity of the positive or negative ion species, v_w is the water velocity and ϕ is the electrostatic potential. From left to right, the terms represent (1) the electric body force on the positive or negative ion, (2) the frictional force of the water on the ion, parameterized by friction coefficients ξ_{\pm} for the cation and anion species and (3) the frictional force of the wall on the ions, parameterized by friction coefficients λ_{\pm} . Note that we have assumed that all of the ions interact appreciably with the walls, a reasonable assumption here given the extreme confinement. We solve for the ion velocity v_{\pm} to obtain:

$$v_{\pm} = \pm \mu_{\pm} (-\partial_x \phi) + \alpha_{\pm} v_w \quad (4)$$

We have introduced the ionic mobilities $\mu_{\pm} \equiv e/(\xi_{\pm} + \lambda_{\pm})$ and the normalized water–ion friction coefficients $\alpha_{\pm} \equiv \xi_{\pm}/(\xi_{\pm} + \lambda_{\pm}) \in (0, 1)$. The former parameters are constrained by the experimental results of ref. ²¹; the latter parameters characterize how effectively the drag of the water flow is able to overcome frictional resistance on the ions from the wall and engender ionic transport. We note that the definition of α_{\pm} may be rearranged to give $\lambda_{\pm}/\xi_{\pm} = (1 - \alpha_{\pm})/\alpha_{\pm}$. This indicates that a value $\alpha_{\pm} \ll 1$ corresponds to stronger ion–wall than ion–water friction, while values of α_{\pm} approaching 1 indicate relatively weaker ion–wall than ion–water interaction.

From the above definitions, we see that the sums of the ion–water and ion–wall friction coefficients are constrained by the experimentally measured mobilities reported in ref. ²¹, $\xi_{\pm} + \lambda_{\pm} = e\mu_{\pm}^{-1}$, while the relative importance of the ion–wall and ion–water interactions, characterized by the ratios $\lambda_{\pm}/\xi_{\pm} = (1 - \alpha_{\pm})/\alpha_{\pm}$, is not.

We next consider the force balance on a control volume of width and height equal to the channel width w and height h , respectively, and of infinitesimal length δx in the along-slit direction. The total volume of the control volume is then $\delta V \equiv wh\delta x$. The total electric body force is given by $e(\rho_+ - \rho_-) \times (-\partial_x \phi) \times \delta V$, and the net pressure force is given by $wh \times (-\partial_x P) \times \delta x$. In the preceding, ρ_{\pm} are the ionic densities (per unit volume) at the position x coincident with the centre of the control volume (so that in the reservoirs $\rho_{\pm} = N_A c$ with N_A the Avogadro number), and P is the pressure. The total frictional force due to ion–wall interactions is $-(\rho_+ \lambda_+ v_+ + \rho_- \lambda_- v_-) \delta V$. Finally, we introduce a coefficient λ_0 characterizing the frictional interaction of water molecules with the walls such that $-\lambda_0 v_w$ is the force per unit wall area acting on the water molecules, and $-\lambda_0 v_w \times w\delta x$ is the total frictional force on the control volume due to water–wall interaction. The force balance on the control volume thus gives:

$$0 = e(\rho_+ - \rho_-)(-\partial_x \phi)\delta V + (-\partial_x P)\delta V - (\rho_+ \lambda_+ v_+ + \rho_- \lambda_- v_-) \delta V - \frac{\lambda_0}{h} v_w \delta V \quad (5)$$

Before solving the above for the water velocity v_w , we use equation (4) and the definitions of μ_{\pm} and α_{\pm} to rewrite the total ion–wall friction force per unit volume δV , $\rho_+ \lambda_+ v_+ + \rho_- \lambda_- v_-$, as:

$$e(\rho_+ - \rho_-)(-\partial_x \phi) - e(\alpha_+ \rho_+ - \alpha_- \rho_-)(-\partial_x \phi) + (\kappa_+ \rho_+ + \kappa_- \rho_-) v_w \quad (6)$$

where we have defined $\kappa_{\pm} \equiv e\alpha_{\pm}(1 - \alpha_{\pm})/\mu_{\pm}$ and made use of the identities $\lambda_{\pm}\mu_{\pm} \equiv e(1 - \alpha_{\pm})$ and $\lambda_{\pm}\alpha_{\pm} \equiv \kappa_{\pm}$. We insert this result into equation (5) and solve for v_w to obtain:

$$v_w = K_{\text{app}}(\rho_+, \rho_-)[(-\partial_x P) + e(\alpha_+ \rho_+ - \alpha_- \rho_-)(-\partial_x \phi)] \quad (7)$$

where $K_{\text{app}}(\rho_+, \rho_-)$ is a concentration-dependent apparent hydraulic permeance, given by:

$$K_{\text{app}}(\rho_+, \rho_-) \equiv \frac{1}{\frac{\lambda_0}{h} + \kappa_+ \rho_+ + \kappa_- \rho_-} \quad (8)$$

To better interpret the significance of the parameter α_{\pm} and the non-intuitive form in which the electric field appears in equation (7), we use the above results to calculate the difference of the electric force f_e^{\pm} and the ion–wall friction force $f_{\text{ion-wall}}^{\pm}$ on a given ionic species:

$$f_e^{\pm} - f_{\text{ion-wall}}^{\pm} = \pm e\alpha_{\pm}\rho_{\pm}(-\partial_x \phi) - \kappa_{\pm}\rho_{\pm}v_w \quad (9)$$

Let us discuss two extreme limits. When $\alpha_{\pm} = 0$, $\xi_{\pm}/\lambda_{\pm} = 0$, indicating that only ion–wall (rather than ion–water) friction is relevant. Further, from the above definition, $\kappa_{\pm} \propto \alpha_{\pm}(1 - \alpha_{\pm}) = 0$, and the net (electric less ion–wall friction) force vanishes. Thus, in this case, all of the electric force on the given ionic species in the control volume is balanced by the strong ion–wall interaction such that the given ionic species does not communicate any electric force to the water molecules. (See equation (7) with α_+ and/or α_- set to zero.)

On the other hand, when $\alpha_{\pm} = 1, \lambda_{\pm}/\xi_{\pm} = 0$, indicating that only ion–water friction is relevant, and all of the electric force on the ions is communicated to the water molecules such that $f_e^{\pm} - f_{\text{ion-wall}}^{\pm} = \pm e\rho_{\pm}(-\partial_x\phi)$. (Again, $\kappa_{\pm} \propto \alpha_{\pm}(1-\alpha_{\pm}) = 0$)

We emphasize that the behaviour described in equations (7) and (8) is in strong contrast to what is observed for conduits with confinement scale (radius or height) greater than about 1 nm, in which the Hagen–Poiseuille equation holds¹⁷. In this case, we would have a concentration-independent permeance $K_{\text{HP}} = h_0/\lambda_0$ and a net electric driving force equal to the total electric driving force $e(\rho_{+}-\rho_{-})(-\partial_x\phi)$. K_{HP} is recovered in the high water friction limit, $\lambda_0/h \gg \kappa_{+}\rho_{+} + \kappa_{-}\rho_{-}$, and both K_{HP} and the total electric driving force are recovered outside of confinement where $\alpha_{\pm} = 1$ (equivalent to no ion–wall friction: $\lambda_{\pm} = 0$).

It is necessary to use equation (7), instead of Hagen–Poiseuille, to capture the full range of qualitative behaviour observed in the experimental $\mu(\Delta V)$ curves. This emphasizes the importance of the two-dimensionality of the flow, resulting in a strong frictional interaction between the channel walls, water and ions.

We insert equation (7) into the general Nernst–Planck parameterization for the ionic fluxes, $j_{\pm} = D_{\pm}(-\partial_x\rho_{\pm}) + v_{\pm}\rho_{\pm}$, to obtain:

$$j_{\pm} = \mu_{\pm} \left[\frac{k_B T}{e} (-\partial_x\rho_{\pm}) \pm \rho_{\pm} (-\partial_x\phi) \right] + \alpha_{\pm} v_w \rho_{\pm} \quad (10)$$

where we have made use of the Einstein relation, $D_{\pm} = k_B T \mu_{\pm}/e$, D_{\pm} being the diffusion coefficients.

At steady state, the conservation equations become:

$$\frac{d(hv_w)}{dx} = 0, \quad \frac{d(hj_{\pm})}{dx} = 0 \quad (11)$$

Finally, the electrostatic potential ϕ is related to the total charge density $e(\rho_{+}-\rho_{-})$ via the Poisson equation:

$$\partial_x [\epsilon\epsilon_0 h(-\partial_x\phi)] = he(\rho_{+}-\rho_{-}) \quad (12)$$

Model geometry and boundary conditions. As we are mainly interested in capturing the qualitative features of the ionic current response, we adopt a simplified one-dimensional geometry. The model geometry adopted here is sketched in Extended Data Fig. 6. A slit of uniform height $h_0 = 7 \text{ \AA}$ and length $L = 5 \mu\text{m}$ connects two reservoirs of divergent geometry. It is necessary to include the reservoirs in some capacity in our calculations to capture the entrance/exit effects associated with the discontinuous change in ionic mobility as the ions enter/exit the channel. The rate of divergence of the reservoir heights is asymmetric, qualitatively mimicking the asymmetry of the experimental geometry. The height profile $h(x)$ is given by:

$$h(x) = \begin{cases} \Gamma_l \left[\left(\frac{x}{L} \right) + \frac{1}{2} \right]^2 + 1, & x \in \left[-\infty, -\frac{L}{2} \right] \\ 1, & x \in \left[-\frac{L}{2}, +\frac{L}{2} \right] \\ \Gamma_r \left[\left(\frac{x}{L} \right) - \frac{1}{2} \right]^2 + 1, & x \in \left[+\frac{L}{2}, +\infty \right] \end{cases} \quad (13)$$

Γ is the rate of divergence of the confinement: the larger Γ is, the more abrupt is the transition to the open reservoir. We take $\Gamma_l = 5$ and $\Gamma_r = 20$. Although the magnitudes of Γ_l and Γ_r influence the quantitative predictions of the model, the qualitative behaviour of the mobilities is similar so long as $\Gamma_l < \Gamma_r$.

We impose the reservoir conditions at $x = \pm\infty$. In the left reservoir, we apply a voltage and pressure:

$$\phi(x = -\infty) = \Delta V \quad (14)$$

$$P(x = -\infty) = \Delta P \quad (15)$$

In the right reservoir, the voltage and pressures are held fixed at reference values arbitrarily set to zero:

$$\phi(x = +\infty) = 0, \quad P(x = +\infty) = 0 \quad (16)$$

The total ionic density in both reservoirs is held fixed at $\rho_{\text{res}} = 2N_A c$, and both reservoirs are assumed to be electroneutral, such that:

$$\rho_{\pm}(x = \pm\infty) = \frac{\rho_{\text{res}}}{2} \quad (17)$$

Variation of ion mobilities μ_{\pm} and normalized water–ion friction coefficients α_{\pm} . We impose the following profiles for the ionic mobilities:

$$\mu_{\pm} = (\mu_{\pm}^{\text{bulk}} - \mu_{\pm}^{\text{conf}}) \left[1 - \frac{\tanh\left(\frac{x + \frac{L}{2}}{\lambda_{\text{adj}}}\right) - \tanh\left(\frac{x - \frac{L}{2}}{\lambda_{\text{adj}}}\right)}{2} \right] + \mu_{\pm}^{\text{conf}} \quad (18)$$

with an adjustment length $\lambda_{\text{adj}} = 0.3 \text{ nm}$. To qualitatively account for the reduction in chloride mobility, we take $\mu_{\pm}^{\text{conf}} = 0.5\mu_{\pm}^{\text{bulk}}$. Similarly, we impose for the normalized water–ion friction coefficients:

$$\alpha_{\pm} = (1 - \alpha_{\pm}^{\text{conf}}) \left[1 - \frac{\tanh\left(\frac{x + \frac{L}{2}}{\lambda_{\text{adj}}}\right) - \tanh\left(\frac{x - \frac{L}{2}}{\lambda_{\text{adj}}}\right)}{2} \right] + \alpha_{\pm}^{\text{conf}} \quad (19)$$

Results. Calculations were performed using the finite element method (COMSOL). Extended Data Fig. 7a–c shows the results of the above model for low water–wall ($\lambda_0/h_0 = 10^{11} \text{ kg m}^{-3} \text{ s}^{-1}$) and water–ion ($\alpha_{+} = 1 \leftrightarrow \lambda_{+}/\xi_{+} = 0$; $\alpha_{-} = 0.7 \leftrightarrow \lambda_{-}/\xi_{-} \approx 0.43$) friction, and Extended Data Fig. 7d–f those for high water–wall ($\lambda_0/h_0 = 10^{13} \text{ kg m}^{-3} \text{ s}^{-1}$) and water–ion ($\alpha_{+} = \alpha_{-} = 0.01$ equivalent to $\lambda_{+}/\xi_{+} = \lambda_{-}/\xi_{-} = 99$) friction. We first note that in both cases we reproduce the linear dependence of the streaming current on the pressure gradient for both zero and non-zero applied voltages (Extended Data Fig. 7b, e), in agreement with experiments (Fig. 3b, c, main text).

The low-friction results produce a quadratic dependence of the streaming mobility on the applied voltage with a minimum mobility occurring for $\Delta V = V_{\min} < 0$ (Extended Data Fig. 7c). This qualitative behaviour is in agreement with the experimental results obtained for graphite (Fig. 3d, main text). Likewise, the high-friction results reproduce the linear dependence of the streaming mobility on ΔV (Extended Data Fig. 7f) that is observed experimentally in hBN (Fig. 3e, main text). The frictional characteristics of these results are consistent with the typically much lower friction (larger slip lengths) observed on graphite than in hBN^{3,22,32}. We note that, in addition to taking low to moderate values of $\lambda_{\pm}/\xi_{\pm} \approx 0\text{--}1$, it is necessary to take $\alpha_{+} > \alpha_{-}$ to recover the qualitative behaviour of graphite. On the other hand, it is necessary to take $\alpha_{+} \approx \alpha_{-} < \sim 0.1$ to recover the qualitative behaviour of hBN. This suggests that frictional interaction of the wall with the ions is weaker generally in graphite, and that it is stronger for chloride than potassium. In hBN, on the other hand, our results suggest that the frictional interaction of the wall with the ions is fairly strong for both species.

The numerical results presented here for the low-friction (graphite-like) configuration indicate that $\mu(\Delta V = 0)$ is independent of concentration, roughly consistent with the minimal variation observed in the experiments (Fig. 2c, main text). However, the linear dependence of the mobility on concentration for non-zero applied voltages (Fig. 3d, e, main text) is not observed in the model (Extended Data Fig. 7c). Conversely, at higher friction (Extended Data Fig. 7d–f), $\mu(\Delta V = 0)$ varies strongly with the concentration, as well as the gated mobility (Extended Data Fig. 7f). This suggests the possibility that the concentration, applied voltage and friction are coupled in ways not accounted for in our simple model.

The numerical results depend crucially on the difference in water flow characteristics between the two materials through the concentration-dependent permeance given in equation (8). However, the nature of this dependence is intricate. Our numerical results indicate that, in addition to the advective current engendered by the applied pressure, the streaming current characteristics depend crucially on the modification of the electrophoretic current $I_{\text{ep}} \propto \rho E$ (figure not shown) via the modification of the concentration and electrostatic fields by coupled voltage and pressure effects. An example of the influence of voltage on the evolution of the concentration fields in the presence of a fixed applied pressure gradient $\Delta P/L = 30 \text{ mbar } \mu\text{m}^{-1}$ and a reservoir concentration $c = 300 \text{ mM}$ is shown in Extended Data Fig. 8c, d. We see that both the applied pressure and voltage induce modification of the concentration profile across the channel (as well as inducing charge separation, not shown). The modification of the concentration profile due to pressure is much stronger in hBN (Extended Data Fig. 8a, c), and it is also much more sensitive to applied pressure and voltage in hBN than in graphite. This latter characteristic is consistent with the smaller streaming mobilities observed in the graphite-like configuration observed in our numerical results (Extended Data Fig. 7c, f). Additionally, we see that the evolution of the concentrations under coupled ΔP – ΔV forcing is different in the two materials; it is this difference, and the corresponding difference in the response of the advective and

electrophoretic currents, that determines the difference between the two material behaviours.

There are several aspects of the observations in graphite that we are not able to reproduce: (1) the non-monotonicity of the dependence of $\mu(\Delta V = 0)$ on concentration, (2) the linear dependence of the mobility on concentration when a voltage is applied and (3) the magnitude of the mobilities measured at high concentration under an applied voltage. Indeed, the model consistently predicts mobilities in the quadratic (graphite-like) regime that are smaller than those observed in the linear (hBN-like) regime (Extended Data Fig. 7c, f). This is not an issue of the voltage range examined, as the mobilities are found to saturate or even reduce at much higher voltages. Likewise, there is much that we have not included in our model: in particular, steric effects and ionic correlations generally, as well as the ‘granular’ nature of water, which might be important at this length scale. Nonetheless, the model does reproduce much of the key qualitative behaviour, and its success depends on the strong differences in the frictional characteristics of hBN and graphite, and further on the incorporation of the retarding influence of the ions on the water transport, an effect that is exclusively two-dimensional. Thus, these results illustrate the two-dimensional character of the flow and the limit of the continuum description of matter.

Geometric sensitivity. The effect of the reservoir geometry on the numerical model predictions is illustrated in Extended Data Fig. 9. In this plot we show the influence of both the relative and absolute magnitudes of Γ_l and Γ_r on the predicted $\mu(\Delta V)$ responses for both the low-friction (graphite-like) and high-friction (hBN-like) configurations. Between the blue and yellow curves, we vary the absolute magnitudes of Γ_l and Γ_r by an order of magnitude while keeping the ratio Γ_l/Γ_r fixed. We see that the magnitudes of Γ_l and Γ_r have no influence on the qualitative (linear or quadratic) behaviour of the mobility curves and have only a slight quantitative influence on the graphite configuration. We also vary the ratio Γ_l/Γ_r (red and purple versus blue and yellow curves). In the graphite response, we see that the minima in the red and purple ($\Gamma_l/\Gamma_r = 1/8$) and the blue and yellow ($\Gamma_l/\Gamma_r = 1/4$) curves are coincident, even as we vary the absolute magnitudes of Γ_l and Γ_r by an order of magnitude. This indicates that in our model, for fixed values of the friction coefficients, the asymmetry determines the location of the minimum mobility

in graphite. Likewise, in the hBN curves, we see that the asymmetry is the only geometric characteristic that determines the slope of the $\mu(\Delta V)$ curve.

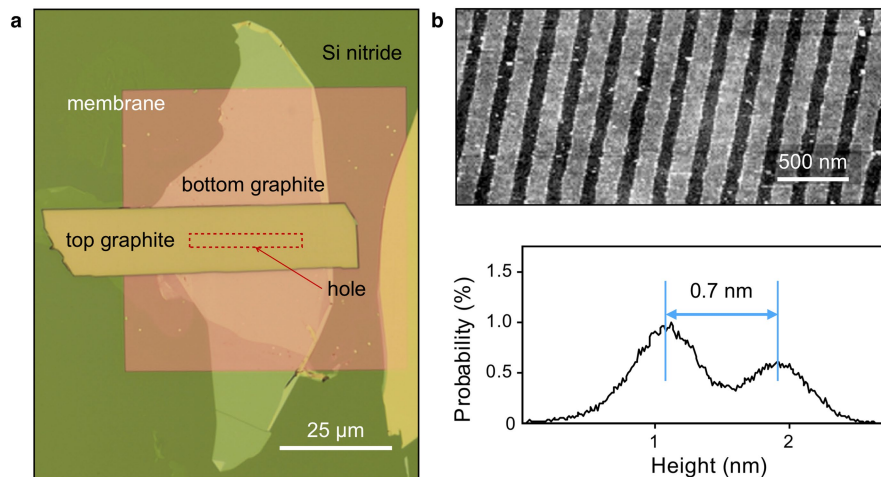
As a final note on the model geometry, a one-dimensional model of the type that we have applied here is strictly valid only if the slope verifies $|\partial_x h| \ll 1$. Formally, this condition is not satisfied deep in the reservoirs. However, variations of the various profiles in the reservoir occur over length scales that are found to be at most of order the channel length L , so that $|\partial_x h| < \Gamma h_0/L$, which remains very small. Note furthermore that reservoirs are included merely to qualitatively capture the influence of (1) the device asymmetry and (2) the entrance/exit effects associated with the abrupt change in anion mobility at the entrance and exit of the slit. Previous work using this approach to include the reservoirs within a one-dimensional PNPS model was successful in capturing the nontrivial qualitative behaviour of the ionic current under applied pressures and voltages³⁴.

Transition behaviour. In Extended Data Fig. 10a–c, we show the influence of the friction parameters for high, low and intermediate friction on the gated mobilities, and in Extended Data Fig. 10d–f we show the relative pressure dependence of the normalized potential $e\Delta\phi/kT$ along the channel axis. $\Delta\phi$ is defined as the potential variation with an applied pressure $\Delta\phi = \phi(\Delta V, \Delta P = 30 \text{ mbar } \mu\text{m}^{-1}) - \phi(\Delta V, \Delta P = 0)$. The modification of the electrostatic potential, and hence the electric field, under coupled pressure–voltage forcing contributes—along with the modification of the concentration field (Extended Data Fig. 8)—to the modification of the electrophoretic current under an applied pressure. Extended Data Figs. 8 and 10 illustrate the complex interplay of competing interactions that contribute to the surprisingly simple linear streaming response observed in the model.

Data availability

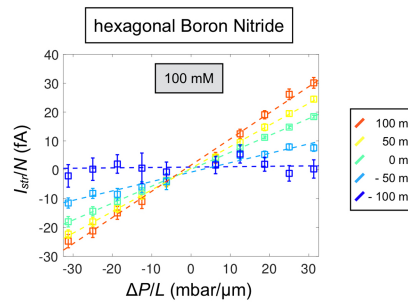
The data that support the plots within this paper and other findings of this study are available in the main text and Extended Data Figures. Additional information is available from the authors upon reasonable request.

34. Jubin, L., Poggioli, A., Siria, A. & Bocquet, L. Dramatic pressure-sensitive ion conduction in conical nanopores. *Proc. Natl Acad. Sci. USA* **115**, 4063–4068 (2018).

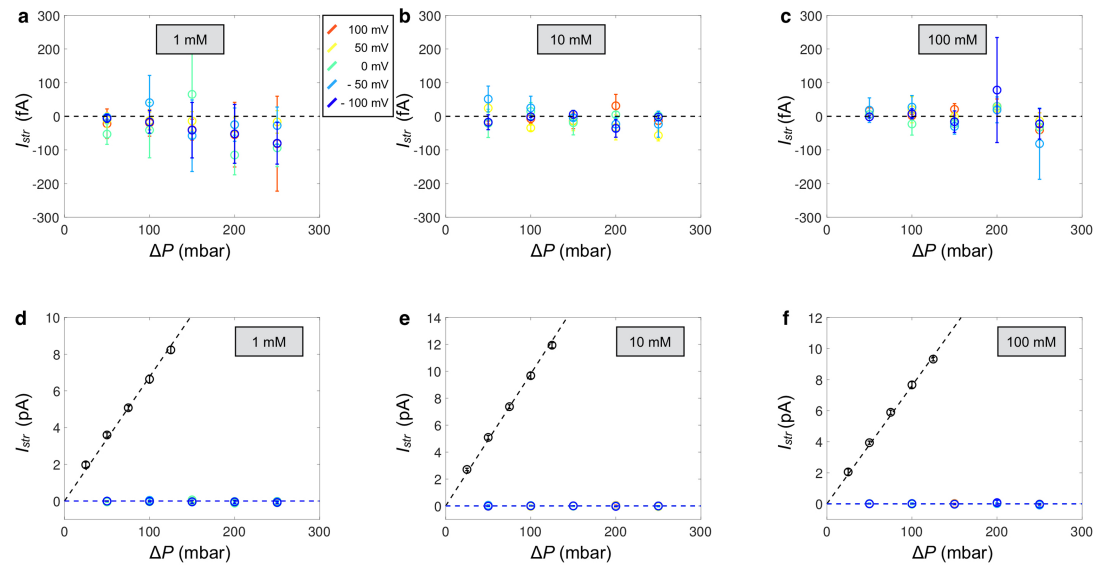


Extended Data Fig. 1 | Ångström-scale channel devices. **a**, Optical image of a device with ångström channels. The square in light pink colour is the silicon nitride membrane which has a rectangular hole shown by the red dotted line. Covering the hole, the bottom graphite layer, spacer and top graphite layer are placed. Bottom and top graphite are visible in the image

in light and bright yellow colours. **b**, Atomic force microscopy (AFM) image of the bilayer graphene spacer lines on the device. The histogram of the heights (below the AFM image) shows that the spacer is about 0.7 ± 0.1 nm thick.

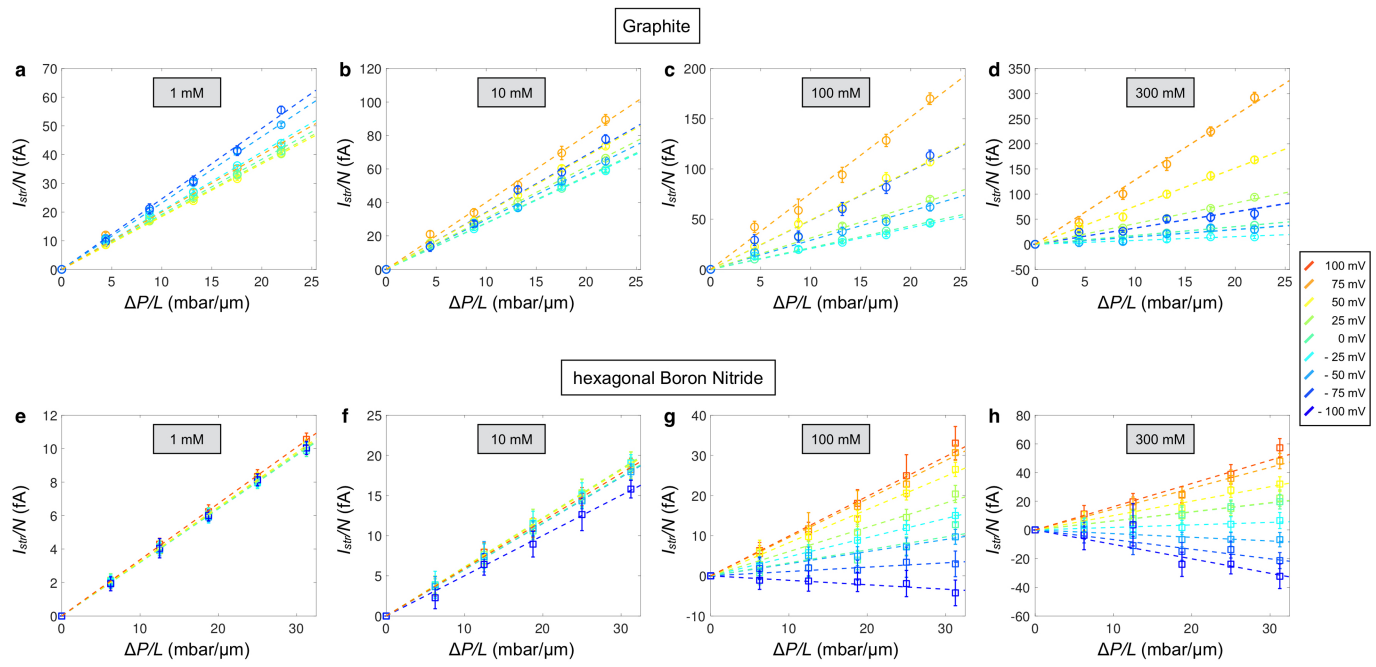


Extended Data Fig. 2 | Gated pressure-driven current. Streaming current per channel plotted as a function of $\Delta P/L$ with ΔV ranging between -100 mV and 100 mV (colour coded from blue to red with increasing voltage difference), KCl concentration of 100 mM and hBN channels of length $L = 16 \pm 0.1$ μ m.



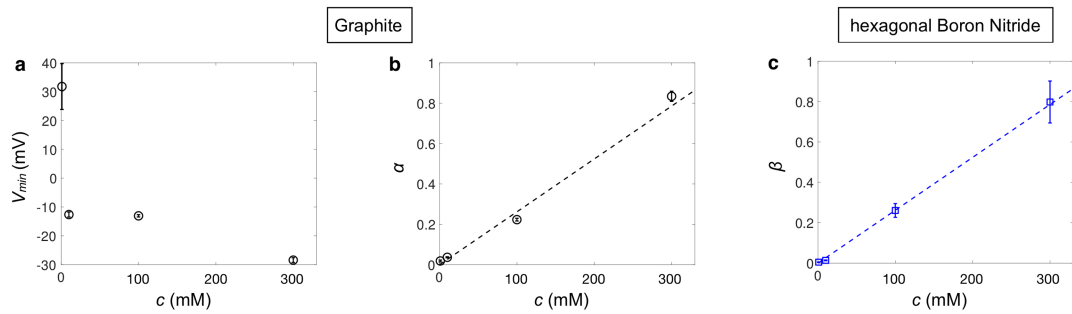
Extended Data Fig. 3 | Control sample test. **a–c**, Streaming current measured in a control sample without any channels as a function of the pressure. We varied the applied voltage from -100 to 100 mV (colour coded from blue to red). **d–f**, Same measurements as for **a–c** (coloured

symbols) but compared with the streaming current measured with 200 graphite channels (black symbols). The streaming current is around 4 orders of magnitude larger, which confirms that channels remain mechanically stable and are not delaminated under pressure.



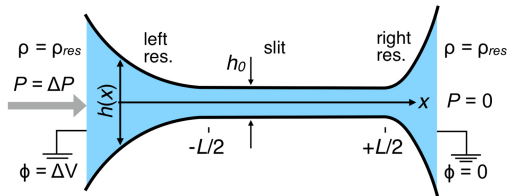
Extended Data Fig. 4 | Gated pressure-driven current and material dependency. Streaming current per channel plotted as a function of $\Delta P/L$ for a KCl concentration varying from 1 mM to 300 mM and with ΔV

ranging between -100 mV and 100 mV (colour coded from blue to red with increasing voltage difference). **a–d**, The channel length L for graphite is 5.7 ± 0.1 μ m. **e–h**, For hBN, $L = 16 \pm 0.1$ μ m.

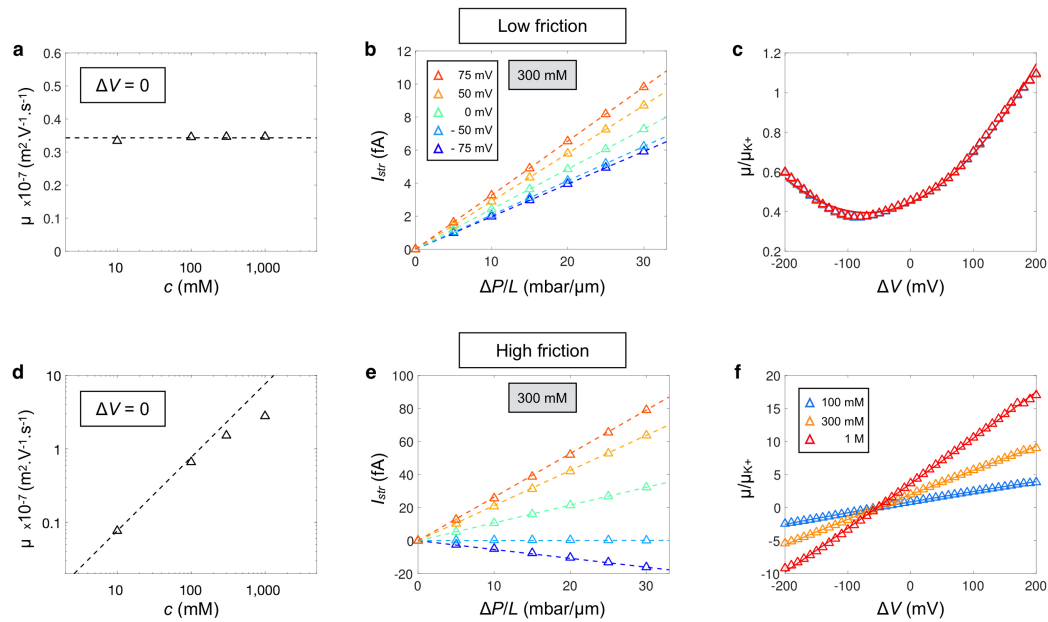


Extended Data Fig. 5 | Concentration dependence of the fit parameters of the gate-controlled mobility. We report the fitting parameters of the voltage-gated streaming current. **a, b,** The quadratic dependence of the gated streaming current observed in graphite channels (Fig. 3d, main text) and described by equation (1): **a**, V_{\min} plotted as a function of the

concentration; **b**, α as a function of the concentration. **c**, We report the fitting parameter β as a function of the concentration for hBN slits: β describes the linear dependence of the streaming current observed for hBN channels (Fig. 3e, main text) as given by equation (2). The dashed lines in **b** and **c** are linear fits.

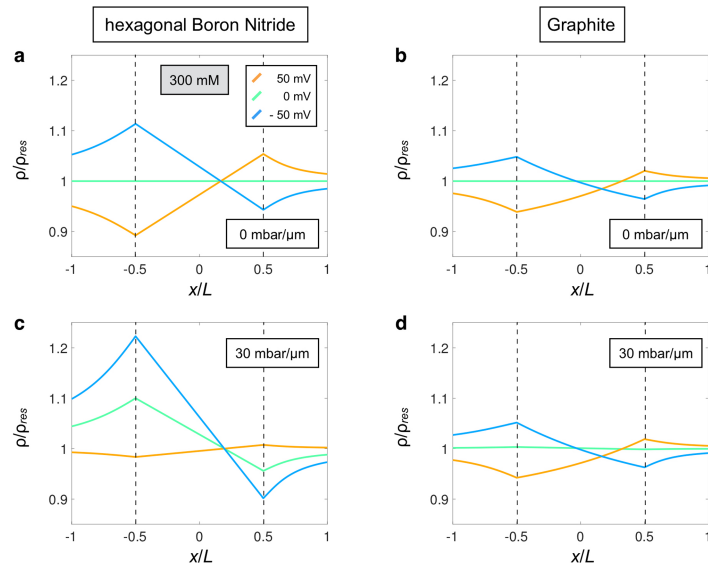


Extended Data Fig. 6 | Geometry and effect of the asymmetry of the system. A slit of uniform height $h_0 = 7 \text{ \AA}$ and length $L = 5 \mu\text{m}$ connects two asymmetric, divergent reservoirs of variable height $h(x)$. The asymmetry in the rate of divergence of the reservoir heights qualitatively mimics the asymmetry of the experimental geometry. A voltage $\phi = \Delta V$ and pressure $P = \Delta P$ are applied in the left reservoir (at $x = -\infty$); the voltage and pressure are held fixed at $\phi = 0, P = 0$ in the right reservoir ($x = +\infty$). The density in both reservoirs is held fixed at $\rho = \rho_{\text{res}}$.



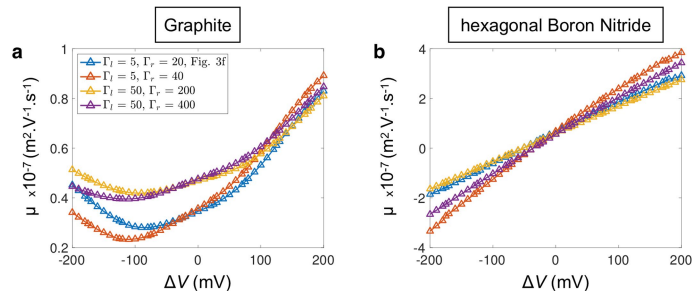
Extended Data Fig. 7 | Prediction of the streaming current from extended Poisson–Nernst–Planck modelling. **a**, Mobility without applied voltage as a function of KCl concentration in linear–logarithmic coordinates for low water–wall friction and $\alpha_+ > \alpha_-$. **b**, Streaming current per channel I_{str} for 300 mM as a function of the pressure gradient $\Delta P/L$ for ΔV varying from -75 mV (blue data) to $+75$ mV (red data). For each voltage, the dashed line corresponds to the linear fit of the data made to extract the mobility. **c**, Streaming mobility μ normalized by the

K^+ electrophoretic mobility μ_{K^+} and plotted as a function of the applied voltage for KCl concentration varying from 100 mM (blue data) to 1 M (red data). **d–f**, Same as in **a–c** but with high water–wall friction and $\alpha_+ = \alpha_-$. Parameters: **a–c**, $\lambda_0/h_0 = 10^{11} \text{ kg m}^{-3} \text{ s}^{-1}$, $\alpha_+ = 1$, $\alpha_- = 0.7$; **d–f**, $\lambda_0/h_0 = 10^{13} \text{ kg m}^{-3} \text{ s}^{-1}$, $\alpha_+ = 0.01$, $\alpha_- = 0.01$. Dashed lines in **a** and **d** are guides to the eye corresponding to a constant value of μ and a linear variation with concentration, respectively.



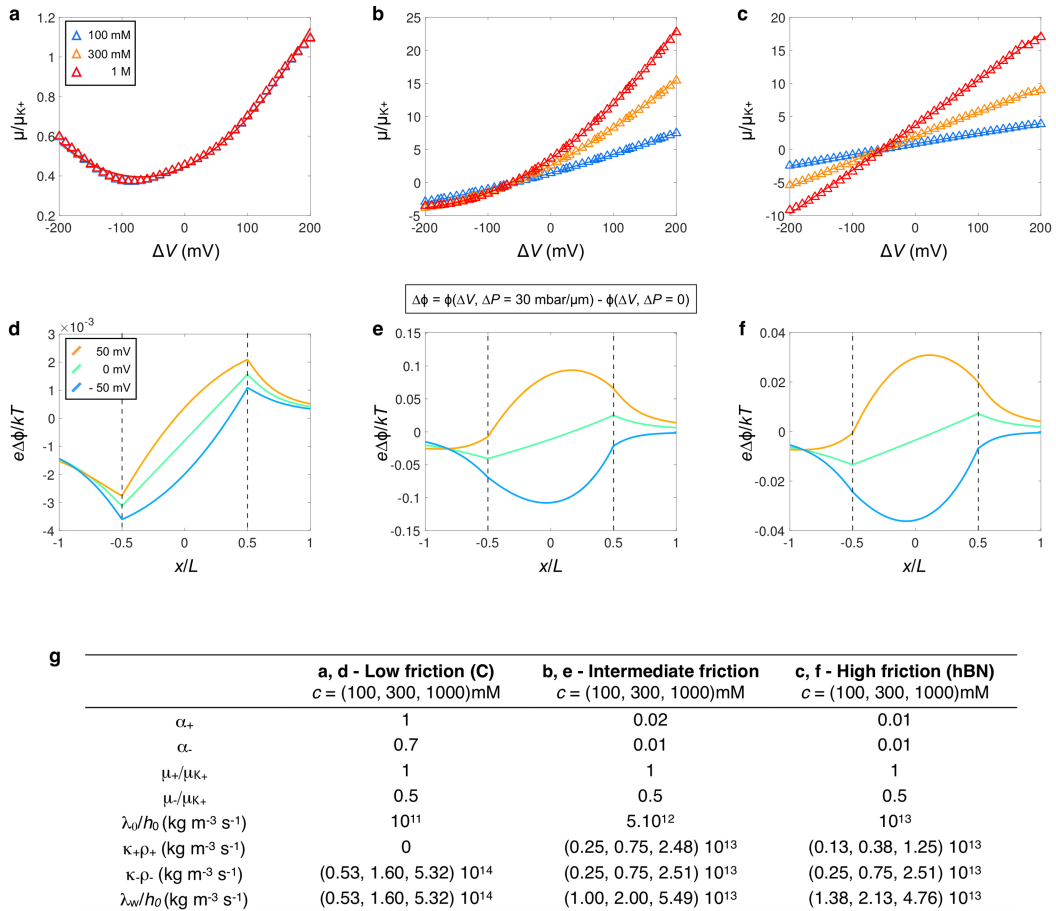
Extended Data Fig. 8 | Total ionic concentration profiles from extended Poisson-Nernst-Planck modelling. **a–d**, Total ionic concentration profiles as a function of the normalized position x/L along the channel without (a, b) and with (c, d) applied pressure for $c = 300 \text{ mM}$. The dashed vertical lines segregate the channel interior, $x/L \in (-0.5, 0.5)$, from the left ($x/L < -0.5$) and right ($x/L > 0.5$) reservoirs. The curves are coloured according

to the applied voltage from -50 mV (blue) to 50 mV (orange). **a**, The high-friction (hBN-like) configuration with $\Delta P/L = 0$. **b**, The low-friction (graphite-like) behaviour with $\Delta P/L = 0$. **c**, The high-friction (hBN-like) configuration with $\Delta P/L = 30 \text{ mbar } \mu\text{m}^{-1}$. **d**, The low-friction (graphite-like) behaviour with $\Delta P/L = 30 \text{ mbar } \mu\text{m}^{-1}$.



Extended Data Fig. 9 | Effect of the asymmetry of the system. **a, b,** Plots show $\mu(\Delta V)$ versus ΔV as a function of asymmetry. **a,** Low-friction (graphite-like) behaviour. In this plot we take $c = 100$ mM, $\alpha_+ = 1$, $\alpha_- = 0.7$, $\mu_+ = \mu_-^{\text{bulk}}$, $\underline{\mu} = 0.5\mu_-^{\text{bulk}}$ and $\lambda_0/h_0 = 10^{11}$ kg m⁻³ s⁻¹, as in the main text, while varying the geometric parameters Γ_l and Γ_r , as indicated

in the legend. **b,** High-friction (hBN-like) behaviour, $c = 100$ mM, $\alpha_+ = 0.01$, $\alpha_- = 0.01$, $\mu_+ = \mu_-^{\text{bulk}}$, $\underline{\mu} = 0.5\mu_-^{\text{bulk}}$ and $\lambda_0/h_0 = 10^{13}$ kg m⁻³ s⁻¹, as in the main text, while varying the geometric parameters Γ_l and Γ_r , as indicated in **a**.



Extended Data Fig. 10 | Influence of the friction parameters on the model predictions. **a–c**, Plots show $\mu(\Delta V)$ versus ΔV for different concentrations ($c = 100\text{ mM}, 300\text{ mM}$ and $1,000\text{ mM}$) and frictional parameters. **a**, Low-friction (graphite-like) behaviour. In this plot, we take $\alpha_+ = 1$, $\alpha_- = 0.7$, $\mu_+ = \mu_+^{\text{bulk}}$, $\mu_- = 0.5\mu_-^{\text{bulk}}$ and $\lambda_0/h_0 = 10^{11}\text{ kg m}^{-3} \text{s}^{-1}$. **b**, Intermediate-friction behaviour, $\alpha_+ = 0.02$, $\alpha_- = 0.01$, $\mu_+ = \mu_+^{\text{bulk}}$, $\mu_- = 0.5\mu_-^{\text{bulk}}$ and $\lambda_0/h_0 = 5.10^{12}\text{ kg m}^{-3} \text{s}^{-1}$. **c**, High-friction (hBN-like) behaviour, $\alpha_+ = 0.01$, $\alpha_- = 0.01$, $\mu_+ = \mu_+^{\text{bulk}}$, $\mu_- = 0.5\mu_-^{\text{bulk}}$ and $\lambda_0/h_0 = 10^{13}\text{ kg m}^{-3} \text{s}^{-1}$. **d–f**, Pressure-induced variation of the normalized electric potential $\Delta\phi = \phi(\Delta V, \Delta P = 30\text{ mbar } \mu\text{m}^{-1}) - \phi(\Delta V, \Delta P = 0)$ plotted as a function

of the normalized channel coordinate x/L axis for $\Delta V = -50\text{ mV}$, 0 mV and 50 mV . The dashed vertical lines segregate the channel interior, $x/L \in (-0.5, 0.5)$, from the left ($x/L < -0.5$) and right ($x/L > 0.5$) reservoirs. The curves are coloured according to the applied voltage from -50 mV (blue) to 50 mV (orange). Panels **d–f** correspond to the parameters of **a–c**, respectively. **g**, Table of the friction parameters corresponding to the data shown in **a–c**. The table also shows the decomposition of $\lambda_w(c)$ into its three components for the concentrations considered here.